Electromagnetic Techniques for Imaging the Cross-Section Distribution of Molten Steel Flow in the Continuous Casting Nozzle

Xiandong Ma, Anthony J. Peyton, Richard Binns, and Stuart R. Higson

Abstract—Control of molten steel delivery through the pouring nozzle is critical to ensure an optimum laminar flow pattern in continuous casting, which influences the surface quality, cleanliness, and hence the value of the cast product. A nonintrusive and nonhazardous visualization technique, which uses rugged and noninvasive sensors, would be highly desirable in such harsh industrial production environments. This paper presents an electromagnetic approach for tomographically visualizing the molten steel distribution within a submerged entry nozzle (SEN). The tomographic system consists of an eight-coil sensor array, data acquisition unit, associated conditioning circuitry, and a PC computer, which have been purposely designed and constructed for hot trials. The paper starts with an overview of electromagnetic imaging techniques. The construction of the sensor array and associated electronics are then discussed, followed by sensitivity map analysis and a description of the applied image reconstruction algorithm. Image results, as reconstructed from cold sample measurements and hot pilot plant trials, are also presented. Despite a low frame acquisition rate (1.35 s per frame), the images generated from the prototype system are capable of providing an adequate representation of the changes of real molten steel flow profiles within the SEN. The paper demonstrates that the application of electromagnetic tomographic technique to this problem shows significant promise for future industrial processes.

Index Terms—Continuous casting, electromagnetic inductance, steel, tomography.

I. INTRODUCTION

IN THE continuous casting of steel [1], control of molten steel delivery through the pouring nozzle, that is, a submerged entry nozzle (SEN) (see Fig. 1), is critical to ensure an optimum laminar flow pattern in the casting mold and stable meniscus. The flow regime in the SEN influences the billet surface quality, cleanliness, and hence the value of the cast product. This is particularly important for casting low carbon aluminum killed steel as the flow profile is readily disrupted by the clogging problem due to the deposition of aluminum oxide particles on the inside of the SEN wall and exit ports [2], [3]. Achievement of a stable and quiescent flow between the tundish and

X. Ma, A. J. Peyton, and R. Binns are with the Engineering Department, Lancaster University, Lancaster LA1 4YR, U.K. (e-mail: x.ma@lancaster.ac.uk; a.peyton@lancaster.ac.uk; r.binns@lancaster.ac.uk).

S. R. Higson is with the Corus RD&T, Teesside Technology Centre, Corus U.K., Ltd., Middlesbrough TS6 6UB, U.K. (e-mail: stuart.higson@corus-group.com).
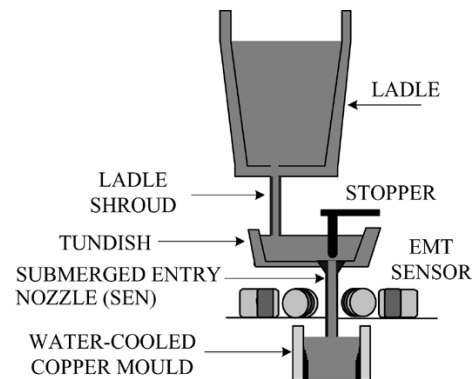
Fig. 1. Location of the submerged entry nozzle in the continuous casting process, where the position of noncontact electromagnetic sensor is also shown.

casting mold is determined by a number of interrelated casting parameters, including steel mass flow rate, tundish metal level [4], pouring nozzle diameter [2], argon gas flow rate [5], and the amount of clogging within the stopper/slide gate and pouring nozzle. Typical examples of steel flow patterns within an SEN are annular flow (a stream with a central air gap), central stream, and bubbly flow (argon bubbles with the stream) with the possible transition between flow modes during casting depending on the flow rate of steel and gas for the given casting conditions. An online flow visualization approach utilizing rugged and noninvasive sensors would be highly desirable.

Much effort has been made in developing a wide variety of tomographic techniques for industrial process applications over the past two decades. For example, the use of X-rays can be considered as a proven method to visualize the flow of liquid steel [6], [7]. However, X-rays suffer from the inherent hazards of radiation and size of the equipment. Electrical techniques have received much attention recently for a number of process applications, especially online monitoring and control, thus providing inexpensive and nonintrusive imaging systems with low, but sufficient, image resolution of the internal material distributions within the processes [8], [9]. Electromagnetic inductance tomography (EMT), which requires custom data acquisition system and physical inductive sensors, uses magnetic coupling between sensors to provide images that represent the distributions of electrically conductive and magnetically permeable material within the object space. This relatively new tomographic technique has been researched for the similar problem of imaging molten metal solidification [10], [11]. Eddy-current techniques have also been utilized in monitoring phase transformation of steel samples in a hot strip mill [12] and character-

izing the Bridgman crystal growth processes by monitoring the liquid–solid interface shape and location [13].

This paper focuses on molten steel flow profile imaging in the continuous casting nozzle based on a prototype EMT instrument. Previous investigative research using a sensor array, consisting of a single transmitter and three pairs of balance coils, has shown that the type of flow profile and flow rate has differentiable effects upon the coil outputs [14], [15]. Central stream flow causes a relatively small signal change in sensor voltage due to the small volume of metal available for eddy-current induction. Bubbly and annular flows are generally large steel bodies, which increase eddy currents, hence signal changes. Bubbly and annular flows can be differentiable at increased operating frequencies as bubbles in the bubbly flow impede the induced eddy-current flow at high frequencies. Previous tests have also shown that a significant reduction in the flow rate produces a partial flow in the pouring nozzle, which results in large variances in signal, as large cavities are sporadically present in the sensor space.

The design of such an instrument must consider the effects of the environment upon the sensor and hence the instrument system. The operational temperature, which varies between 1000–1500 °C, demands that the sensor array should be low cost, easily maintainable, and constructed from materials capable of enduring such high temperatures. Low-input capacitance is essential in order to maximize the resonant frequency. However, long cables, which are generally required between the sensor array and instrument during hot trails, introduce extra input capacitance, thus reducing the resonant frequency of the system. The pouring nozzle wall will induce eddy currents when an alternating magnetic field is incident due to the material being electrically conductive; this affects the selection of the optimum excitation frequency.

This paper starts with an overview of electromagnetic imaging techniques. The construction of the sensor array and associated electronics are then discussed, followed by sensitivity map analysis and a description of the applied image reconstruction algorithm. Images, as reconstructed from cold sample measurements and hot pilot plant trials, are presented. This paper will be the first to present tomographically reconstructed images of real molten steel flows through a submerged entry nozzle. The aim of such a system is to determine, and ultimately visualize, steel flows within the SEN from which flow regime knowledge is created, thus enabling improved control over casting conditions.

II. EMT

EMT, also termed mutual inductance tomography (MIT) [16], [17], maps spatial distribution of electrical conductivity or magnetic permeability through the measurement of magnetic coupling between inductive sensors. The underlying principle behind the technique can be described generally as follows: The object space is energized with a sinusoidally varying magnetic field created through excitation coils. Electrically conductive or ferromagnetic objects inside the space causes distortion to the magnetic field due to induced eddy currents in the test objects. The resultant field changes are measured on the object space periphery with an array of detection coils. The corresponding voltage measurements are fed into a PC host computer. Based on a series of measured coil outputs and through utilizing reconstruction algorithms, the PC computer is able to produce an image of the internal material distribution. Molten steel is a conductive media as the temperature exceeds the Curie point and cannot be detected magnetically as it displays no magnetic properties [12]. The electrically conductive molten steel causes a reduction in the detected signal due to Faraday's law and therefore only the electrical conductivity is imaged.

For EMT, the forward problem is to predict the sensor outputs for a given material distribution with known electromagnetic properties. Analytical approaches are suitable for solving forward problems for ideal geometries with simplified assumptions; numerical approaches, such as finite-element methods (FEM), are used to calculate approximately the forward problems in the general case. The inverse problem, through the utilization of image reconstruction techniques, is to convert the measured data into an image which represents the original material distribution. The reconstruction problem of conductivity mapping in EMT is an ill-posed and ill-conditioned problem as the number of pixels in an image is usually much larger than the number of the limited measurements. This problem is further complicated by the soft field effect, whereby the object material affects both the magnitude and direction of the interrogating field. Therefore, the measured induced voltage is a nonlinear function of electrical conductivity of the test objects. There is no direct approach to solving this inverse problem. It is generally necessary to use nonlinear reconstruction methods such as the regularized Gauss–Newton methods to achieve desirable images where each step in such an iterative method is treated as a regularized linear step [18].

However, assumptions are made of the system that simplifies the image reconstruction problem. Assuming the system to be linear so that pixel interactions are ignored, which is a very coarse approximation to reality, the system is described by a matrix equation

$$\mathbf{z} = \mathbf{S} \cdot \mathbf{k} \tag{1}$$

where $\mathbf{z}$ is the measurement data and $\mathbf{k}$ the image pixel values. Vector $\mathbf{k}$ contains N elements, the total number of pixels in the object space, whereas vector $\mathbf{z}$ contains M elements, which represents the total number of independent measurements, i.e., the number of unique coil pairs to be measured. The two-dimensional matrix $\mathbf{S}$ of M rows and N columns contains the sensitivity coefficients, which reflect the response of each pixel to a particular measurement.

For the image reconstruction problem as described in (1), the pixel contrasts in $\mathbf{k}$ need to be solved as the measured vector $\mathbf{z}$ and the sensitivity matrix $\mathbf{S}$ are already known. However, a reconstruction algorithm is required as the inverse of matrix $\mathbf{S}$ is not directly available. There is a range of possible EMT reconstruction algorithms [19]; however, for this project, a Simultaneous Increment Reconstruction Technique (SIRT) was employed, which is detailed in the following section.
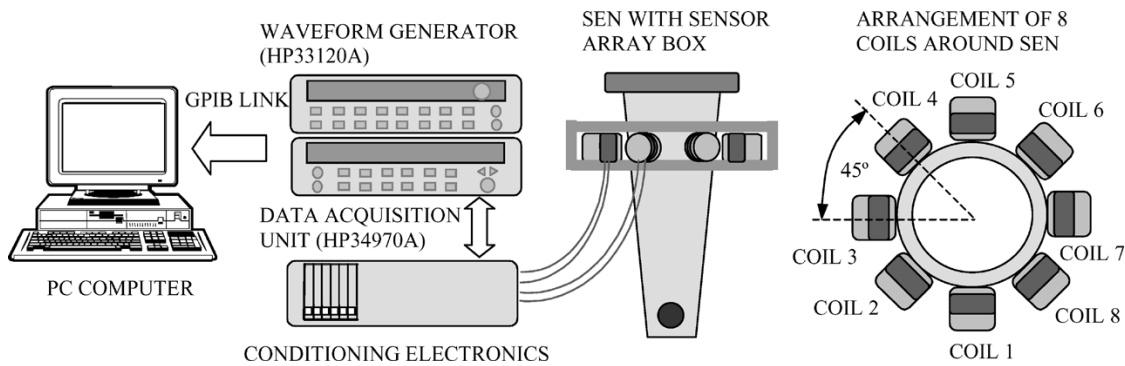
Fig. 2. Block diagram of the experimental system. The system consists of a sensor array, data acquisition unit, associated conditioning circuitry, and a PC computer, which were purposely designed and constructed for hot trials.

III. EMT IMAGING SYSTEM

A. Experimental System

The initial investigative system based on an impedance analyzer approach proved that the use of electromagnetic approaches to visualize simple geometries was possible [14], [15]. However, an automated system is required for hot pilot plant trials. The instrument system, as schematically illustrated in Fig. 2, was designed and constructed to achieve the hot test aims. The 5-kHz 10-V ac signal is provided from a Hewlett Packard waveform generator. The conditioning electronics convert the 5-kHz voltage source to a current signal, which is driven at 300 mA to provide the coil excitation signal. The conditioning electronics also performs the demodulation of current signal and induced voltages from the detection coils with respect to excitation waveform, producing in-phase and quadrature dc components. The data acquisition unit has three tasks: the switching of the excitation signal via reed relays to each coil sequentially, control over amplitude gain selection of 1, 56, 226, and 362 depending on the detection coil position relative to excitation coil, and converting the resolved dc components to digital signals. The data acquisition software is realized in Visual C++ making use of the Microsoft Foundation Class (MFC) library in conjunction with General Purpose Interface Bus (GPIB) and Virtual Instrument Software Architecture (VISA) library to facilitate nine-channel data loggings (excitation current and eight detection voltages). A Pentium-based PC computer operating the online acquisition software takes the readings via a GPIB link and stores the data in formats suitable for retrieval by software packages such as MATLAB for further imaging processing. The system has a frame acquisition rate of approximately 1.35 s.

In order to select the optimum excitation frequency, the penetration effect of eddy currents into the pouring nozzle, which is typically graphite-alumina, must be considered. The electrical conductivity of graphite is $\sigma \approx 70$ kS/m compared to $\sigma \approx 2.1$ MS/m for steel at room temperature and $\sigma \approx 800$ kS/m for molten steel at 1500 °C. The penetration of eddy currents into the pouring nozzle is frequency dependent. It was found that the nozzle attenuated the eddy-current signal at frequencies above 10 kHz. To avoid significant eddy-current losses in the nozzle walls, its operating frequency should be limited to below 10 kHz. Therefore, 5 kHz was selected as the operating
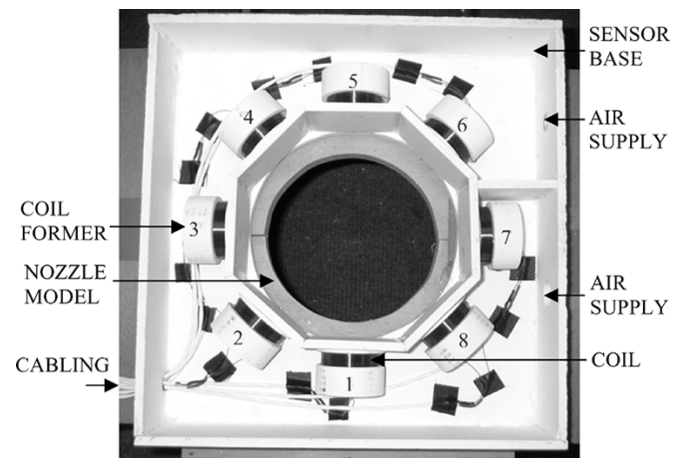

Fig. 3. Photograph of the physical sensor and nozzle model.

frequency at which the skin depth was 26.9 mm for graphite so that the nozzle had a negligible effect compared to the nozzle wall thickness (17 mm). In the meantime, the skin depth for molten steel at 1500 °C was 8.0 mm, which was comparable with object space size to ensure that a sufficient volume of steel was probed.

The main sensor array components are eight coils, which were chosen as a compromise between system complexity and image resolution. Each coil was wound with copper wire (50 turns, 50-mm diameter each) and equally spaced at 45° intervals around the periphery of the SEN to preserve symmetry. Each coil, together with its associated electronics, can be multiplexed between excitation and detection tasks as directed by the PC computer. At each projection, one coil is energized while the remaining seven coils act as detectors. The quadrature signals are measured as they provide larger voltages, hence improved signal-to-noise ratio (SNR). Coils are energized in sequence to provide a total of eight projections and hence 56 measurements. However, only 28 independent measurements are used for each frame image reconstruction due to sensor coil reciprocity.

Fig. 3 shows a photograph of the physical sensor and nozzle model. The nozzle has an inner diameter of 70 mm, which represents the maximum area to be visualized. Naturally, the materials for sensor array construction must be carefully selected to endure the high temperatures during hot tests. A machinable ceramic material (Duratec 750) was used to construct the coil
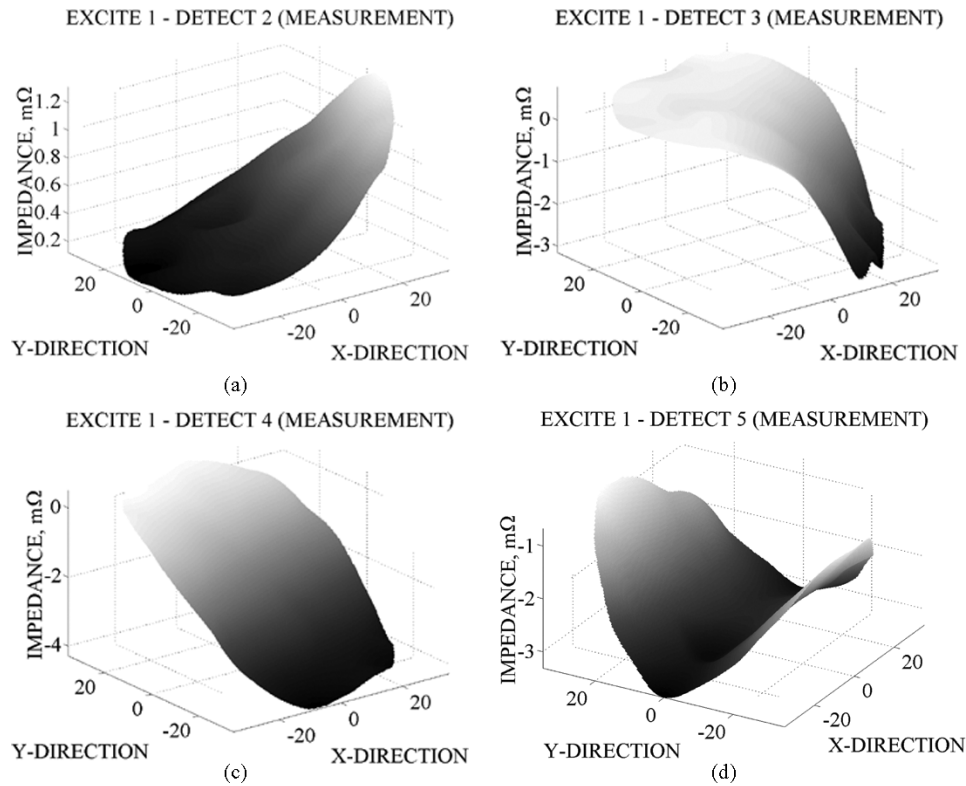
Fig. 4. Four measured primary sensitivity maps for a symmetrical eight-coil sensor array system, all dimensions in X and Y directions are in millimeters. (a) Sensitivity map for excitation coil 1 and detection coil 2. (b) Sensitivity map for excitation coil 1 and detection coil 3. (c) Sensitivity map for excitation coil 1 and detection coil 4. (d) Sensitivity map for excitation coil 1 and detection coil 5.

formers, array base, and enclosure as shown in Fig. 3, which operated at 1000 °C. Silicone sealant was utilized to bond the sensor array as it also had a high temperature rating (300 °C). After assembly, the coils were boxed with a central area empty to accommodate the nozzle. An air supply was applied to the enclosure passing through the coils for cooling; the internal temperature was monitored.

B. Sensitivity Maps

The sensitivity maps, which are dependent on the material distribution in the sensor array, show spatial sensitivity of a particular excitation-detection coil combination to pixel perturbations within the object space. Sensitivity maps are widely used to solve the inverse problems in image reconstruction, as they describe the unique conductivity distribution to pixel perturbations for the given sensor array. These maps can be calculated by either analytical approximation [20], numerical approaches, or by experimental measurements. In this case, sensitivity maps were produced using direct measurements and compared with FEM simulations.

In the experimental measurements, a copper rod ($\sigma \approx 58$ MS/m) of 12.5-mm diameter was used to represent the pixel perturbation. The rod was placed and moved upon a 10-mm grid inside the nozzle model. A square area of 49 pixels, a 7×7 matrix, was therefore required to describe the nozzle's 70-mm diameter circular space; this required 37 individual rod positions. Only perturbations with respect to empty space were considered. The response to empty space, under identical excitation conditions, was subtracted from the outputs of a

detector coil when the target rod was present, i.e., (1) becoming $\Delta \mathbf{z} = \mathbf{S} \cdot \Delta \mathbf{k}$; thus, only net effects caused by the target object were recorded. To minimize the unwanted interference effects, nine scans were taken upon the detection coil voltage for each perturbation for averaging purposes. Impedance changes were calculated by dividing the averaged voltage changes and the associated current readings.

In image reconstruction, it is normally necessary to calculate the primary sensitivity maps due to sensor array symmetry, and all of the other maps can be derived from these by rotational transformations. Fig. 4 shows four primary maps for the eight-coil sensor array, which represent the changes in the imaginary component of the mutual impedance of each coil pair. The initial maps have 37 pixels; hence, the maps have been smoothed and interpolated for adequate presentation. This process consists of a square 7×7 matrix generation from the initial 37 pixels by placing corner pixels via simple averaging of the nearest pixels, followed by both X and Y direction interpolations onto a 200×200 pixel grid using cubic spline operations. A circular map is finally constructed using 31 415 pixels of the available 200×200 pixels. The smoothness in the shape of the maps illustrates the minimal effect of noise upon the system. As expected, for opposite coils (1 and 5, refer to Fig. 3 for coil positions), a distinctive saddle shape is observable. The map shapes of other coil pairs (1 and 2, 1 and 3, 1 and 4; see Fig. 3) show that the increase in the magnetic field coupling is apparent when the perturbation approaches the coils.

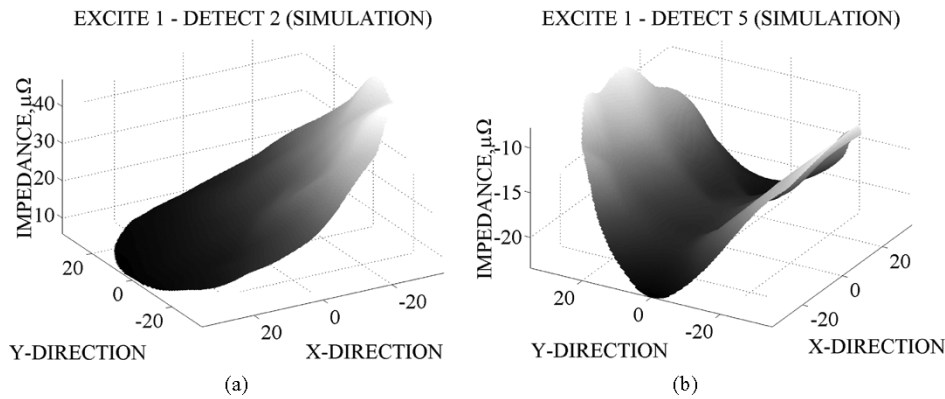For the comparison, the sensor array, as shown in Fig. 3, was simulated using Maxwell (Ansoft Corporation), which is

Fig. 5. Simulation sensitivity maps of coil pairs when coil 1 is excited using Maxwell (Ansoft Corporation). All dimensions in X and Y directions are in millimeters. (a) Neighboring coil pairs 1 and 2 and (b) opposite coil pairs 1 and 5.

a three-dimensional (3-D) finite element package, to create the simulated sensitivity maps. This simulation software offered a piecewise solution to field problems by splitting the problem into a series of small tetrahedral elements over which the field values are approximated. A problem region was solved of five times the size of the sensor model to ensure that the applied boundary conditions did not over constrain the solution. The surrounding air was assigned by the material property of a vacuum. A total of 21 558 tetrahedral elements were meshed to ensure that the simulations converged to 0.5% error.

As with the experimental method, a 12.5-mm diameter copper rod was used as the target object and moved upon a 10-mm grid inside the nozzle. At each rod position, the coils were excited with a 5-kHz 300-mA sinusoidal current; Maxwell calculated the induced voltages on the sensing coils under each excitation both with and without a perturbation object inside, respectively. The time expense required for computing a full collection of 56 maps on a Pentium PC (2.20 GHz CPU, 2.0 GB RAM) was approximately 81 h. This meant that an average time of approximately 90 min was taken for one sensitivity map calculation, which was much longer than the experiment method.

Fig. 5 shows the simulated sensitivity maps, as the examples, between neighboring coil-pair (coil 1–2) and opposite coil-pair (coil 1–5). The shape similarity between the simulated and experimental maps can be measured in terms of cross-correlation coefficients. Unrelated maps result in a correlation coefficient of zero, whereas equivalent maps have a correlation coefficient of one. The correlation coefficients between Figs. 4(a) and 5(a) and Figs.4(d) and 5(b) are 0.8526 and 0.8105, respectively. In addition, the normalized dot division of the simulated and experimental maps shows that all the dot values are between 0.5 and 1.0. All of these indicate that the simulated and experimental maps for the same coil pair are in good agreement. The differences are mainly due to the significant approximations made in the simulation, for example, a single stranded turn for coils in the simulation system rather than 50 turns for coils in the real system, and the gain control, which is normally used in the instrument system for the induced voltage amplification depending on the coil pair position relative to the nozzle.

The final sensitivity matrix represents an amalgamation of a series of the sensitivity maps and has dimensions of 28×49,

where 28 represents M elements in matrix $\mathbf{S}$ and 49 denotes N elements in matrix $\mathbf{S}$. An experimental sensitivity matrix was employed during image reconstruction.

C. Image Reconstruction

The SIRT reconstruction algorithm involves an iterative process to solve the equation as described in (1) for $\mathbf{k}$ when $\mathbf{S}$ and $\mathbf{z}$ are known. The iterative algorithm at step i is described by

$$\mathbf{k}^{(i+1)} = \mathbf{k}^{(i)} + \lambda(\mathbf{z} - \mathbf{S} \cdot \mathbf{k}^{(i)}) \cdot \mathbf{B} \qquad (2)$$

where $\mathbf{B}$ represents the backward projection matrix and λ is the relaxation factor that controls the convergence speed of the algorithm. Matrix $\mathbf{B}$ could use heavily regularized inverse matrices, for example, based on truncated singular value decomposition (SVD) [18]. However, in this case, a normalized transposition of $\mathbf{S}$ is used, namely $\mathbf{B_j} = \mathbf{S_j^T} \times \|s_j\|^{-2}$ $(0 \le j \le N)$, as it is a simplistic method for converting measurements into images. An initial guess $\mathbf{k}^{(0)}$ is made for $\mathbf{k}$. As only conductive media is present, nonnegative constraining is used to limit the value of each pixel to lie between zero and one, where the maximum value of one corresponds to a full element and values between zero and one to partially filled elements [15].

Cold samples were initially employed to determine the ability of the system and reconstruction algorithm in distinguishing between differing areas of conductivity. Titanium rods (electrical conductivity $\sigma = 2.1$ MS/m) were used as test phantoms for real problem imitation. Three titanium rods with known sizes of 19-, 25-, and 35-mm diameters were placed at different positions within the nozzle. Fig. 6 shows the responses in time sequence of coil 5 acting as a detector under excitation of coil 1, as an example, to three rods at different positions. It is evident that a larger rod causes larger signal changes in the induced voltage due to larger eddy-current losses. For a given phantom, the smallest signal change is found at the center position; this is in agreement with previously presented sensitivity maps. A difference in signal between positions 1 and 3 for the largest rod is possible due to misalignment during these tests.

Fig. 7 shows images of three rods placed in different positions in the pouring nozzle by utilizing the measured coil outputs in conjunction with the SIRT algorithm, where λ and the
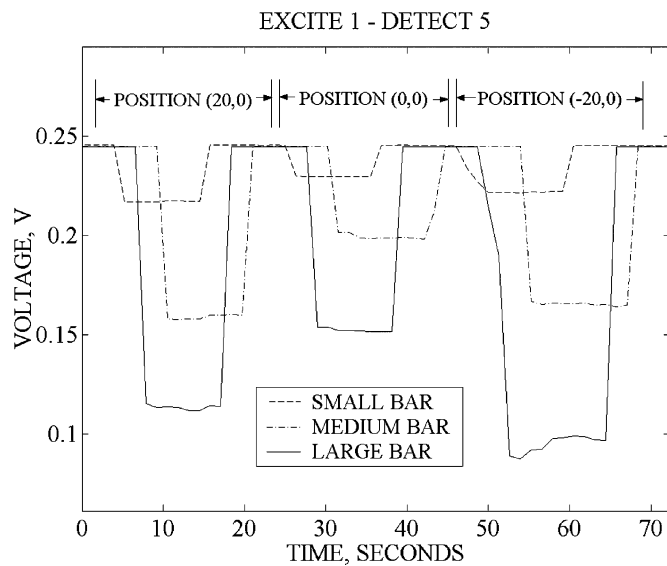
Fig. 6. Coil outputs in time sequence for small (19-mm diameter), medium (25-mm diameter), and large (38-mm diameter) rods placed at three different positions within the nozzle. Larger rod causes larger signal changes of the induced voltage due to larger eddy-current losses, and central position suffers from the least spatial resolution.

number of iterations are 0.01 and 2000, respectively, which are the case dependent. From these images, there is good accuracy between real and estimate rod positions. The relative sample size can be inferred by comparing the pixel value differences of the three rods. As a further example, Fig. 8 shows an image of three copper rods (two 19-mm-diameter rods and one small 12.5-mm-diameter rod) placed within the nozzle. The inference of the sample size becomes difficult as the magnetic field coupling between rods complicates the problem more than in the single-rod case. However, the position predictions are in good agreement with the real positions.

IV. HOT PLANT TRIAL RESULTS

Hot casting trials were undertaken using the heavy pilot plant facilities at Corus Teesside Technology Centre. The trial arrangement is shown in Fig. 9. The sensor array was placed around a transparent quartz glass tube, which was positioned off center (top right), within a standard slab caster SEN and connected to the EMT instrument through long thermally shielded cables, which suffered no degradation of signal over the required 7 m. Molten steel was supplied from a 4-ton nominal capacity electric arc furnace via a stoppered ladle to a tundish and then passed to a pseudo-casting mold via the glass tube to enable submerged pouring to be simulated. Two scans were taken for averaging purposes, which resulted in a sampling rate of 2.70 s/frame. Casting was maintained for approximately 220 s. During data loggings, flow patterns were also observed and recorded using video.

Fig. 10 shows the sensor outputs throughout casting for the cases of a neighboring coil-pair (coil 1–2) and an opposite coil-pair (coil 1–5). The short step changes of the detected signal are the indicators of casting commencing and casting stopping during pouring. Two breaks in casting are observed in the illustration, which were manually established by controlling
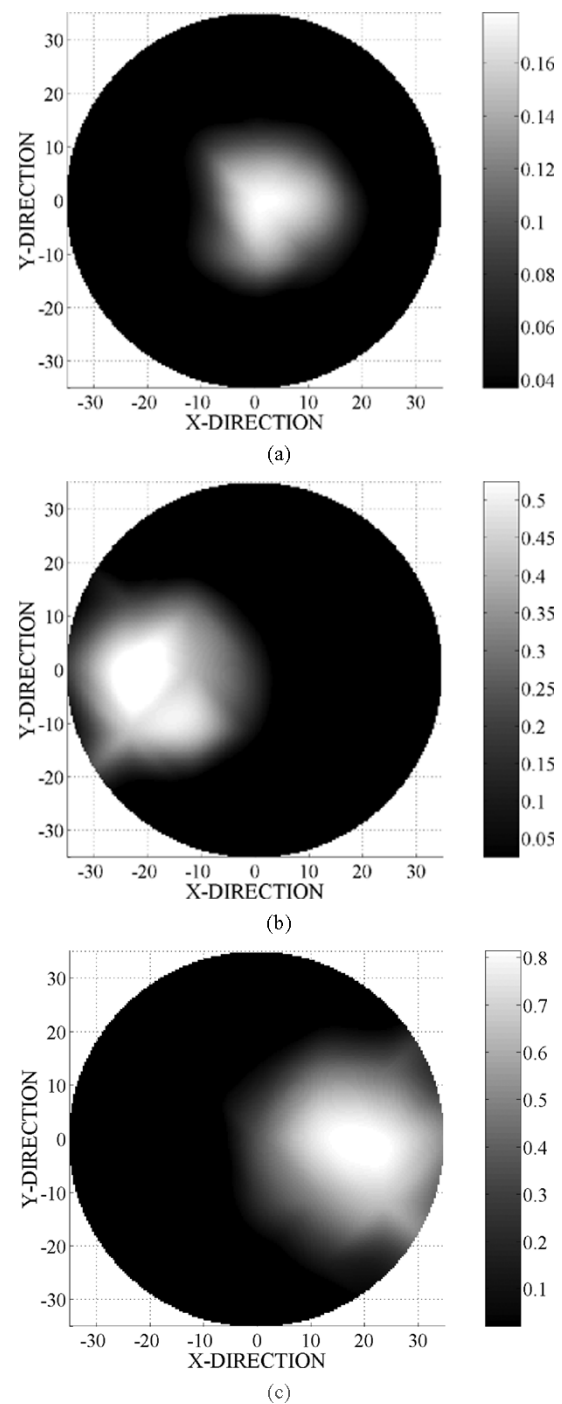

Fig. 7. Images of small (19-mm diameter), medium (25-mm diameter), and large (38-mm diameter) titanium rods: (a) small rod at (0,0), (b) medium rod at (−20,0), and (c) large rod at (20,0).

the stopper rod. Thermal drift is apparent in the detected signal compared with the coil response to cold samples as shown in Fig. 6; this is possibly caused by the combination of drift of the sensing electronics and thermal variations in the EM properties of the support materials. The resultant signal appears as if a thermal-free signal is superimposed on a background signal, which changes exponentially with casting time. This background signal is thereby numerically fitted with an exponential curve and then subtracted from the original detected signal to
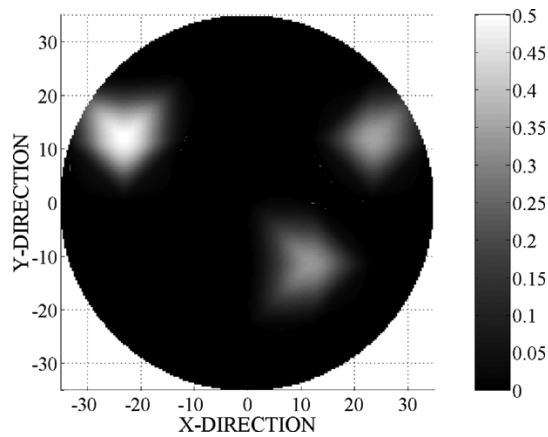
Fig. 8.   Images of two copper rods (19-mm diameter at (−20, 10) and (10, −10), respectively) and one small copper rod [12.5-mm diameter at (20, 10)] when placed within nozzle simultaneously.
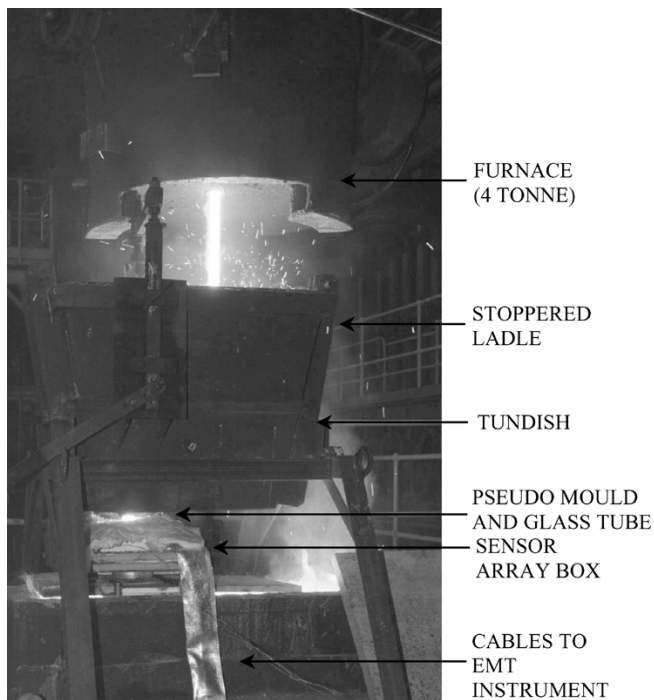

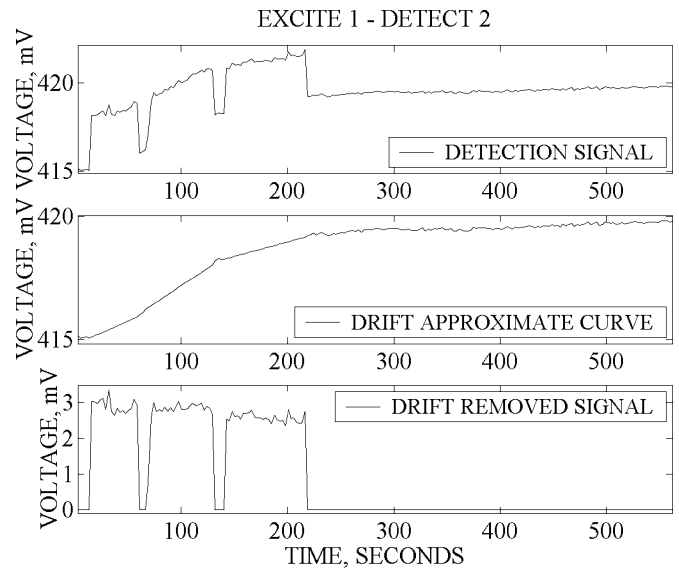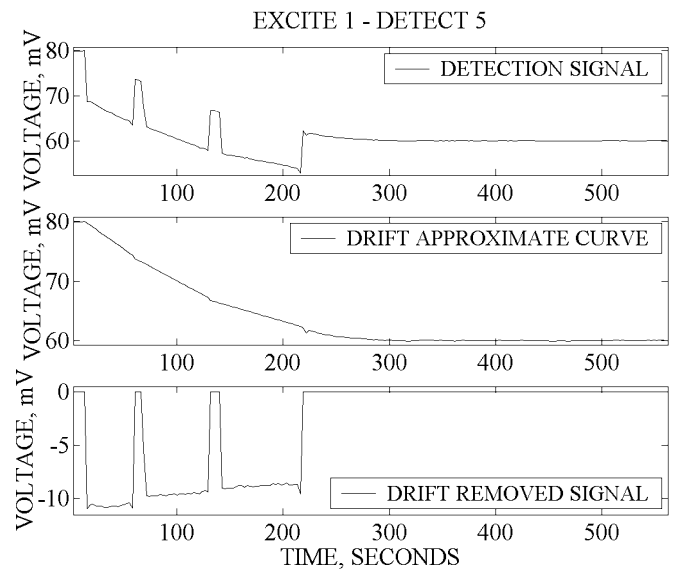Fig. 9.   Hot casting trials using the pilot plant facilities at Corus Teesside Technology Centre.

Fig. 10.   Display of the detected signals during hot trial and thermal drift effect removal: (a) coil 2 excited by coil 1 and (b) coil 5 excited by coil 1.

achieve a thermal-free signal. All sensor outputs are treated accordingly to remove thermal effects.

The thermally compensated outputs are arranged in a matrix such that the rows represent the time sequence, i.e., image frame index, and the columns the coil-pair measurements respectively. Images of steel flow profiles are then produced by utilization of the reconstruction algorithm with $\lambda = 0.01, 2500$ iterations and nonnegative constraining. More iterations are used due to a reduction in the SNR of hot trial signals. A selection of results is shown in Fig. 11. The images are shown in sequence from left to right and then top to bottom with a common gray scale. All images adequately predict the position, i.e., the upper right side of the SEN. The two breaks in the pour at approximately 65 and 140 s are clearly visible. The changes of steel flow profiles can

be differentiated in terms of the variation in grey level which lies at the right of each image.

It is evident that these images provide a good representation of the steel flow profile changes through the SEN during casting. The results were consistent with video recording of an exposed section of the steel flow. Consequentially, the hot trial results demonstrate that the electromagnetic sensing technique can be used to monitor and visualize the real molten steel flow through a pouring nozzle.

V. CONCLUSION

The paper has presented an EMT system, which is composed of an eight-coil sensor array, a data acquisition unit, the associated conditioning circuitry, and a PC-based computer. The system has been purposely designed and constructed for hot plant trials. A suitable excitation frequency is selected for the
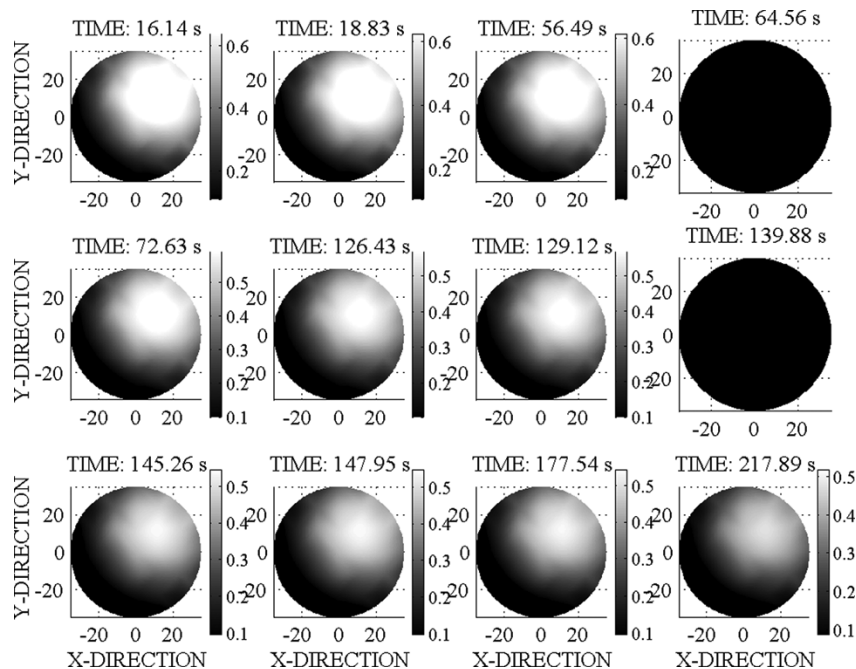
Fig. 11. Images of molten steel flow profiles through the SEN during hot trial at different time instants; two stops are also included (black images). Changes of steel flow profiles can be differentiated in terms of the variation in grey level which lies at the right of each image.

system, at which the conductive nozzle has little effect upon field penetration. Images from the cold sample tests show that the object position can be discriminated and the inference of the relative object size is possible. The promising results from the preliminary pilot plant trials demonstrate that the EMT approach can be utilized to monitor and visualize real molten steel flow through a pouring nozzle.

The present system uses a simple reconstruction algorithm for image reconstruction and has a low data acquisition rate (1.35 s per frame). An improved EMT system is under development to increase acquisition speed, decrease system size, improve resolution, and present the images in real time. An improved reconstruction algorithm, based on nonlinear regularised techniques, such as Gauss–Newton methods, is also being formulated for hot trial measurement data. Also, as single frequency excitation has been shown to inadequately resolve complex flow regimes, a multifrequency measurement approach and a subsequent inversion algorithm is required to offer a solution capable of visualizing complex annular and bubbly flows within the nozzle. Nevertheless, it is believed that the EMT application holds significant promise for the future industrial process.
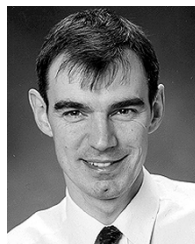
ACKNOWLEDGMENT

REFERENCES

[1] X. Ma, A. J. Peyton, R. Binns, and S. R. Higson, "Imaging the flow profile of molten steel through a submerged pouring nozzle," in *Proc. 3rd World Congr. Industrial Process Tomography*, Banff, AB, Canada, 2003, pp. 736–742.
[2] F. G. Wilson, M. J. Heesom, A. Nicholson, and A. W. D. Hills, "Effect of fluid flow characteristics on nozzle blockage in aluminum killed steels," *Ironmaking Steelmaking*, vol. 14, pp. 296–309, 1987.
[3] H. Yin, H. Shibata, T. Emi, and M. Suzuki, "Characteristics of agglomeration of various inclusion particles on molten steel surface," *Iron Steel Inst. Japan Int.*, vol. 37, pp. 946–955, 1997.
[4] F. L. Kemeny, "Tundish nozzle clogging: Measurement and prevention," in *Proc. Mclean Symp.*, 1998, pp. 103–110.
[5] H. Bai and B. G. Thomas, "Effects of clogging, argon injection and continuous casting conditions on flow and air aspiration in submerged entry nozzles," *Metallurg. Mater. Trans. B*, vol. 32, pp. 707–722, 2001.
[6] M. Hytros, I. Jureidini, D. Kim, J. H. Chun, R. Lanza, and N. Saka, "A computed tomography sensor for solidification monitoring in metal casting," in *Proc. TMS Annu. Meeting Materials Processing*, 1997, pp. 173–181.
[7] M. Hytros, I. Jureidini, J. H. Chun, R. Lanza, and N. Saka, "High-energy x-ray computed tomography of the progression of the solidification front in pure aluminum," *Metallurg. Mater. Trans. A*, vol. 30, pp. 1403–1410, 1999.
[8] W. Q. Yang, A. L. Stott, M. S. Beck, and C. G. Xie, "Development of capacitance tomographic imaging systems for oil pipeline measurements," *Rev. Sci. Instrum.*, vol. 66, pp. 4326–4332, 1995.
[9] M. Wang, A. Dorward, D. Vlaev, and R. Mann, "Measurements of gas-liquid mixing in a stirred vessel using electrical resistance tomography (ERT)," *Chem. Eng. J.*, vol. 77, pp. 93–98, 2000.
[10] M. H. Pham, Y. Hua, and N. Gray, "Imaging the solidification of molten metal by eddy currents – Part 1," *Inv. Probl.*, vol. 16, pp. 469–482, 2000.
[11] ——, "Imaging the solidification of molten metal by eddy currents—Part 2," *Inv. Probl.*, vol. 16, pp. 483–494, 2000.
[12] S. Johnstone, R. Binns, A. J. Peyton, and W. D. N. Pritchard, "Using electromagnetic methods to monitor the transformation of steel samples," *Trans. Instrum. Meas. Contr.*, vol. 23, pp. 21–29, 2001.
[13] K. P. Dharmasena and H. N. G. Wadley, "Eddy current sensor concepts for the Bridgman growth of semiconductors," *J. Crystal Growth*, vol. 172, pp. 303–312, 1997.
[14] R. Binns, A. R. A. Lyons, and A. J. Peyton, "Imaging of steel profiles within a pouring nozzle," in *Proc. 2nd World Congr. Industrial Process Tomography*, Hanover, Germany, 2001, pp. 138–145.
[15] R. Binns, A. R. A. Lyons, A. J. Peyton, and W. D. N. Pritchard, "Imaging molten steel flow profiles," *Meas. Sci. Technol.*, vol. 12, pp. 1132–1138, 2001.
[16] A. J. Peyton, Z. Z. Yu, G. Lyon, S. Al-Zeibak, J. Ferreira, J. Velez, F. Linhares, A. R. Borges, H. L. Xiong, N. H. Saunders, and M. S. Beck, "An overview of electromagnetic inductance tomography: Description of three different systems," *Meas. Sci. Technol.*, vol. 7, pp. 261–271, 1996.
[17] H. Griffiths, "Magnetic induction tomography," *Meas. Sci. Technol.*, vol. 12, pp. 1126–1131, 2001.

[18] W. R. B. Lionheart, "Reconstruction algorithms for permittivity and conductivity imaging," in *Proc. 2nd World Congr. Industrial Process Tomography*, Hanover, Germany, 2001, pp. 4–11.

[19] A. R. Borges, J. E. Oliverira, J. Velez, C. Tavares, F. Linhares, and A. J. Peyton, "Development of electromagnetic tomography (EMT) for industrial applications, Part 2: Image reconstruction and software framework," in *Proc. 1st World Congr. Industrial Process Tomography*, Buxton, U.K., 1999, pp. 219–225.

[20] A. J. Peyton, S. Watson, R. J. Williams, H. Griffiths, and W. Gough, "Characterising the effects of the external electromagnetic shield on a magnetic induction tomography sensor," in *Proc. 3rd World Congr. Industrial Process Tomography*, Banff, Canada, 2003, pp. 352–357.

Anthony J. Peyton received the B.Sc. (first class) degree in electrical engineering and electronics and the Ph.D. degree from the University of Manchester Institute of Science and Technology (UMIST), Manchester, U.K., in 1983 and 1986, respectively.

He was appointed a Principal Engineer at Kratos Analytical, Ltd., in 1989, developing precision electronic instrumentation systems for the magnetic sector and quadrupole mass spectrometers, from which an interest in electromagnetic instrumentation developed. He returned to UMIST as a Lecturer and worked with the Process Tomography Group. He moved to Lancaster University, Lancaster, U.K., with his research team, in 1996, as a Senior Lecturer. He was promoted to Reader in electronic instrumentation in July 2001 and to Professor in May 2004. His main research interests include the areas of instrumentation, applied sensor systems, and electromagnetics.

Xiandong Ma received the B.Eng. degree in electrical engineering from Jiangsu University of Science and Technology, China, in 1986, the M.Sc. degree in power systems and automation from Nanjing Automation Research Institute (NARI), China, in 1989, and the Ph.D. degree in partial discharge detection and analysis from Glasgow Caledonian University, U.K., in 2003.

Between 1989 and 1998, he worked with NARI as an Electrical Engineer for eight years and later as a Senior Engineer for two years, developing DSP-based power system real-time digital simulators dedicated for close-loop power equipment testing. He has been a Research Associate at Lancaster University, Lancaster, U.K., since 2002, and his current research interests include electromagnetic induction tomography for industrial process, nondestructive testing, and instrumentation.

Richard Binns received the M.Eng. degree in mechatronics and the Ph.D. degree from Lancaster University, Lancaster, U.K., in 1998 and 2002, respectively.

After working for 18 months at a defense company, which specialized in radar products, he accepted a Research Associate position at Lancaster University. He is currently investigating the implications of using ultrawide-band radar to detect and image various materials and geometries.

Stuart R. Higson graduated from Sheffield University, U.K., in 1988.

He then joined British Steel, Teesside Technology Centre, subsequently Corus, U.K., Ltd., Middlesbrough, U.K., where he has worked mainly in the area of developing novel steel casting techniques. These studies have included direct strip casting using the twin roll technique and steel flow visualization in the submerged entry nozzle.